Feasibility of Using Orbital Resonances for Nearby Stars to Constrain the Triaxiality of the Galactic Halo

Casper Hesp

Bachelor thesis under supervision of Amina Helmi

Kapteyn Institute, University of Groningen

March 2015, Groningen

ABSTRACT

Based on exploratory simulations, Rojas-Niño et al. (2012) have proposed that triaxiality in the Galactic dark matter halo might cause lumpiness in the velocity distribution of halo stars in the Solar Neighbourhood through orbital resonances. Accordingly, they have asserted that detecting the presence of substructures in velocity space may be a method for diagnosing the shape of the dark matter halo of the Milky Way. However, this conclusion is based on a somewhat idealized initial configuration. In the current study, a more realistic set-up for the initial conditions was used to simulate the kinematic effects of a triaxial NFW halo (Vogelsberger et al. 2007) on halo stars in a galaxy similar to the Milky Way. We found the local velocity distributions in our simulations to be relatively smooth. Although resonances were indeed present and associated with specific regions of velocity space, they did not leave visible imprints in the form of substructures. It appears that only the shape of the velocity ellipsoid is significantly affected by triaxiality. We conclude that a method based on the identification of resonant orbital families in velocity space will probably not be sensitive enough for testing triaxiality of the dark matter halo of the Milky Way.

Subject headings: dark matter halo, Milky Way, orbital resonances, stellar kinematics, triaxiality

Acknowledgements

First and foremost I would like to express my gratitude to my thesis supervisor, Amina Helmi, who has provided me with this project and has guided me throughout the process. She has made the effort to introduce me to the research field of galactic dynamics and welcomed me into her research group. Her expertise, sharp perception, and numerous comments have been essential for attaining the current academic level of my research as a whole.

Secondly, I would like to thank both Robyn Sanderson and Maarten Breddels for providing their source codes and helping to adjust these codes for application in this project. Their comments and availability for discussion have been very helpful to me.

Lastly, I would like to thank the Kapteyn Institute and the University of Groningen for providing me with the right academic environment and the computational power needed for the numerical experiments of my project.

Contents

1 Introduction **4**

2 Method **7**

2.1 General Procedure 7

2.2 Initial Conditions 7

2.3 The Triaxial NFW Potential 15

2.4 Derivation of the Equations of Motion 19

2.5 Leapfrog Integrator 20

2.6 Kullback-Leibler Divergence 22

2.7 Characterization of Orbital Resonances 25

3 Results **29**

3.1 Overall Local Velocity Distributions 29

3.2 Statistical Tests on Local Velocity Distributions 34

3.3 Resonance Populations Identified with Fourier Analysis 37

3.4 Resonance Populations in Velocity Space 42

4 Discussion **46**

References **51**

1. Introduction

The cosmological model that currently seems to be the most successful in explaining the formation of structure in the Universe is the Lambda Cold Dark Matter (ΛCDM) model (e.g. Cole et al. 2000), in which Λ denotes the infamous cosmological constant representing dark energy. According to this model the baryonic components of galaxies are embedded in dark matter halos. Since dark matter particles interact extremely weakly, the evolution equations of the system are solely determined by gravitational forces. This is a text-book example of an N-body problem which makes for convenient study of the structure and properties of dark matter halos with N-body simulations. The Aquarius project (Springel et al. 2008) conducted one of the largest N-body simulations ever of the formation of a Milky Way-like halo within the ΛCDM. Their simulations confirmed one characteristic that has been found earlier in numerical studies within ΛCDM (e.g. Allgood et al. 2006), namely that the dark matter halos show triaxiality which changes with time and distance from the halo center (for in-depth analysis on halo shape evolution, see e.g. Vera-Ciro et al. 2011).

Constraining the exact shape of the dark matter halo of our Milky Way and its orientation relative to the Sun has proven to be a difficult task. For example, one complication is that the simulations in Vera-Ciro et al. (2011) predict the halo shape itself to be dependent on radius. Therefore its gravitational effects on baryonic matter are expected to vary with radius and this complicates pinning down the exact form of the potential using the still sparsely available data. The largest obstacle right now is the lack of precision in measuring the positions and velocities of stars in the stellar halo. This is expected to greatly improve with the upcoming data from the Gaia project (Perryman et al. 2001).

Nonetheless, several different methods have already been designed to measure the shape of the dark matter halo of the Milky Way. One that has been extensively applied

concerns fitting the Sagittarius tidal stream (e.g., Law et al. 2009). By now, results seem to converge tentatively on an almost fully oblate halo whose minor axis is oriented towards the Sun (Law & Majewski 2010). However, this form does not correspond with predictions based on simulations like Aquarius (Vera-Ciro & Helmi 2013) in which dark matter halos have three different axis scales, i.e. they are triaxial.

A case analogous to that of constraining the halo shape concerns constraining the parameters of the Galactic bar. According to e.g., Monari et al. (2012), one promising approach for determining the parameters of the bar is to analyze substructures in the velocity distributions of stars of the Galactic disk in the Solar Neighborhood. These substructures can be related to orbital resonances caused by the Galactic bar which introduces a non-axisymmetric component to the potential. These authors have made simulations of the Galactic disk which have shown that specific orbital resonances with the bar give rise to substructure in the velocity space of the disk stars. With thoroughly detailed information on the velocities of the disk stars, one could constrain the parameters describing the bar. By analogy, this case of deviation from axial symmetry due to the Galactic bar can be extended to the deviation from spherical or axial symmetry due to triaxiality of the Galactic halo. In this way, triaxiality of the dark matter halo might induce substructure in the local velocity distribution of halo stars which in turn might be observable.

In search of more ways to constrain the parameters of triaxiality, Rojas-Niño et al. (2012) have explored this idea which lead to their premise that structure in the local stellar kinematics might actually be the 'smoking gun' for detecting halo triaxiality. Their simulations showed that triaxiality in the Galactic dark matter halo might indeed induce substructure in the velocity distribution of stars in the Solar Neighbourhood (SN) due to orbital resonances. However, for the sake of computational efficiency they did not

attempt to accurately represent the orbital structure of the Galactic halo and their method overselected stars populating orbital resonances. Therefore, feasibility of the proposed strategy remains to be tested with realistic simulations. The question remains whether the local velocity distribution would be perturbed strongly enough by the orbital resonances to provide practically useful constraints to the axis ratios of the halo. This is the purpose of the current study. We outline our procedure in general in Section 2.1. The justifications for the choice of initial conditions, the used potential, corresponding equations of motion, and the integrator are treated in Sections 2.2 to 2.5. We discuss the statistical method and the characterization of the orbital resonances in Sections 2.6 and 2.7. Sections 3.1 and 3.2 are devoted to the velocity distributions and the results of the corresponding statistical tests. The orbital analyses are outlined in Sections 3.3 and 3.4. Finally, in Section 4 the findings will be discussed, compared, and contrasted with those of Rojas-Niño et al. (2012).

2. Method

2.1. General Procedure

Firstly, we generate initial phase-space coordinates for a spherical distribution of halo stars. Then we integrate the stars in triaxial, oblate, and prolate NFW-potentials. After integration, we select stars from five different SN-like regions, located on the major, intermediate, and minor axes and slightly off-axis for the major and minor directions. For these stars, we perform statistical tests to determine the significance of substructures in velocity space. We then use spectral orbit classification to identify the different orbital resonances and types of orbits. Finally, we link this information back to the velocity distributions in order to analyze their relationship. All these steps are outlined in more detail in the following sections.

2.2. Initial Conditions

Initially we construct a stellar halo to resemble the six-dimensional phase-space structure of the stellar halo of the Milky Way in the idealised case of spherical symmetry. We choose pure sphericity for the initial potential so that all observed effects can be traced back to the triaxiality of the imposed potential. Although it is highly unlikely that any halo will be initially formed in a spherically symmetric potential, this does not reduce generality since we are interested in investigating the influence of triaxiality by itself on orbital structure. Since according to the ΛCDM (Cole et al. 2000) most of the mass in our Milky Way is made up of cold dark matter (CDM), we assume that the mass of the test-particles themselves does not contribute significantly to the potential. Accordingly, we choose the potential that has been generally found to be produced in cold dark matter simulations with ΛCDM. It has been named NFW after the authors of the classic paper in

which it was proposed (Navarro, Frenk, White, 1997):

$$\Phi_{NFW}(r) = -\frac{GM_{200}}{r_s f(C_{200})} \frac{\ln(1 + r/r_s)}{r/r_s} \tag{1}$$

Here $f(u) = \ln(1+u) - u/(1+u)$, the scale radius is denoted by r_s, and the concentration parameter $C_{200} = r_{200}/r_s$, which is taken to be ~ 10 for a galaxy with a mass similar to that of the Milky Way (Hayashi et al. 2007). r_{200} is the virial radius, which is defined as the radius of a sphere within which the mean density of the distribution is equal to 200 times the critical cosmological density ρ_c for closure. M_{200} is defined as the total mass within this radius, the virial mass, which is $\sim 8 \times 10^{11} M_\odot$ for the Milky Way(e.g., Battaglia et al. 2006; Busha et al. 2011; Cautun et al. 2014).

To produce a mock stellar halo similar to that of the Milky Way, we will use the method of Sanderson et al. (2014). We first assign orbital energies to the stars by selecting their apocenter distances, r_a, in a way that reproduces observed distributions. According to Kinman et al. (1994), the number density distribution of stars in the primary halo follows the power law $\rho \propto r^{-3.5}$. If we assume that the average mass per star does not vary with apocenter radius, we find that the mass density and probability density distributions as functions of r_a are linearly related to each other. Therefore $p(r_a)dV \propto \rho(r_a)dV \propto r_a^{-3.5}dV$. After setting the inner radius to 0.3 kpc to avoid divergence of the integral and using $dV = 4\pi r_a^2 dr_a$, we can integrate this equation to find the normalization factor. The resulting probability distribution for r_a is:

$$p(r_a)dr_a = \frac{1}{2}\sqrt{\frac{r_c}{r_a^3}}dr_a \tag{2}$$

From this distribution we draw the apocenter radii with the extra condition that 3 kpc $< r_a <$ 100 kpc to avoid the type of orbits that are too close or too far to be relevant for our analysis which concerns the SN at $\sim$ 8 kpc from the Galactic center. Due to the spherical symmetry of the system the spatial angles were distributed uniformly in θ and ϕ

$(-\pi < \theta < \pi; 0 < \phi < 2\pi)$. The resulting density profile is shown in the left panel of Figure 1.

Now that we have set up the spatial coordinates, we are going to generate the initial velocities which point in the tangential direction since the radial velocities are zero at the apocenters. Since the gravitational force in the radial direction is given by $F_{r,g} = -\frac{\mathrm{d}\Phi}{\mathrm{d}r}$ and the centrifugal force by $F_{r,cf} = \frac{v_c^2}{r}$, an expression for the circular velocities can be derived:

$$v_c^2 = r\frac{\mathrm{d}\Phi}{\mathrm{d}r}. \tag{3}$$

Therefore, we take the derivative of the NFW potential (1) with respect to r:

$$\frac{\mathrm{d}\Phi}{\mathrm{d}r} = \frac{GM_{200}}{r^3 f(C_{200})}\left(\ln\left(1 + r/r_s\right) - \frac{r/r_s}{(1 + r/r_s)}\right) \tag{4}$$

Combining with equation (3) gives us:

$$v_c^2 = \frac{GM_{200}}{r^2 f(C_{200})}\left(\ln\left(1 + r/r_s\right) - \frac{r/r_s}{(1 + r/r_s)}\right) \tag{5}$$

We use this relationship to determine the angular momentum of a circular orbit, L_c, associated with a given r. These values can then be related to the total orbital angular momenta by choosing the circularity parameter $\eta \equiv L/L_c(r_a)$ from a distribution derived from simulations by Wetzel (2011). Orbital circularity is defined as the ratio of the total angular momentum of an orbit to that of a purely circular orbit that has the same energy. Those authors fitted a function to the circularity distribution of infalling objects which has the following form:

$$f(\eta) = C_0 \eta^{1.05}(1 - \eta)^{C_1} \tag{6}$$

Functions for the parameters C_0 and C_1 were also fitted by Wetzel (2011), which for our case (assuming redshift $z \sim 0$) give us $C_0 = 5.3$ and $C_1 = 0.813$. We generate values for the cumulative probability between 0 and 1 from a uniform probability distribution and then use it to solve Equation (6) numerically to produce the associated η values. The resulting

probability distribution for η is shown in Figure 2. After finding these values, the total orbital angular momenta L can be derived using the definition of $\eta \equiv L/L_c(r_a)$.

Since at their apocenters r_a the radial velocities V_r for all test particles are zero, the only non-zero velocity component is the tangential one and therefore $V_t = L/r_a$. Due to sphericity of the potential the velocities are uniform in ζ which is defined as the angle in the tangential plane. Therefore, corresponding velocities in the spherical coordinates are $V_\theta = V_t \sin\zeta$ and $V_\phi = V_t \cos\zeta$.

We use this method to produce the six-dimensional phase-space coordinates of two million test particles. The fact that all orbits are generated at the apocenter distances r_a is not expected to influence the simulation results given that enough integration time is taken to allow for phase-mixing to take place. After a test integration in the spherical potential, we fit the number density distribution to confirm that it indeed follows the power law $\rho \propto r^{-3.5}$. This is plotted in the right panel of Figure 1.

We select spherical regions with radii of 2 kpc that could possibly represent our Solar Neighborhood (within which phase-space coordinates can be determined observationally) at a distance of 8 kpc from the center of the halo on the three main axes and near the major and minor axes ($\sim$ 14 degrees off-axis; see Figure 3) of the triaxial NFW-potentials in which the particles are going to be integrated. The initial velocity distributions within the volumes from Figure 3 can be seen in Figure 4. The velocity dispersions are the smallest ($\sigma_{min} = \sigma_{V_r} \sim 5$ km/s) in the direction parallel to the radial direction of the centers of the regions. This is to be expected because the initial radial velocities are zero. This also means that the velocity dispersions must be the largest in the directions perpendicular to the radial direction of the centers of the regions, i.e. the tangential direction. This can be confirmed by looking at Figure 4, where indeed $\sigma_{max} = \sigma_{V_t} \sim 56$ km/s. These dispersions are for the extreme case in which all particles are at their apocenters simultaneously.

Therefore it is more relevant to check the distribution after phase-mixing the orbits by integrating them in a spherical NFW-potential. As seen in Figure 5, $\bar{V_r} = \bar{V_\theta} = \bar{V_\phi} \sim 0$ km/s, $\sigma_{V_r} \sim 70$ km/s, and $\sigma_{V_\theta} = \sigma_{V_\phi} \sim 80$ km/s. After phase-mixing, we expect σ_{V_r} to be larger than its initial value. We see that σ_{V_r} is slightly smaller than σ_{V_θ}. One cause of this might be that the peak of the probability distribution of the circularity (see Figure 2) lies slightly to the right, i.e. favoring orbits with higher circularity which contribute more to σ_{V_θ} than to σ_{V_r}. The overall velocity dispersions are smaller than the dispersions for halo stars in the Solar Neighborhood. This is what we expected because we have not included the disk component of the Milky Way which would increase the velocity dispersions.

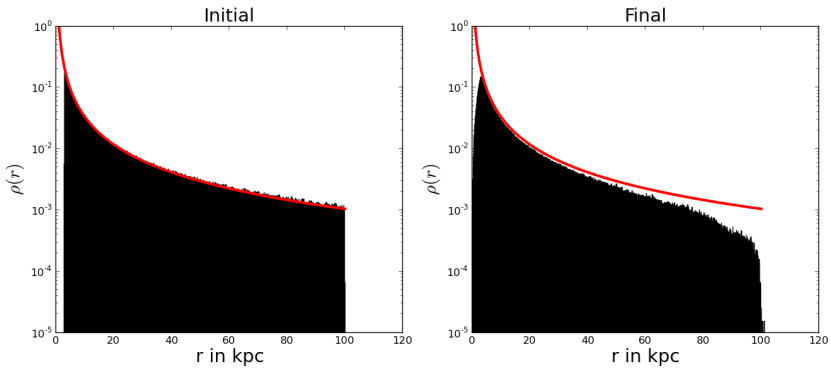

Fig. 1.— The normalized density profile as a function of radius for the initial conditions and after integrating for 8 Gyr in the triaxial NFW-potential. The defined distribution $\rho \propto r^{-3.5}$ is plotted with a red line. Because all stars began at the apocenters of their orbits, it is expected that the stars will populate more the inner regions after integration which is also seen in the figure.

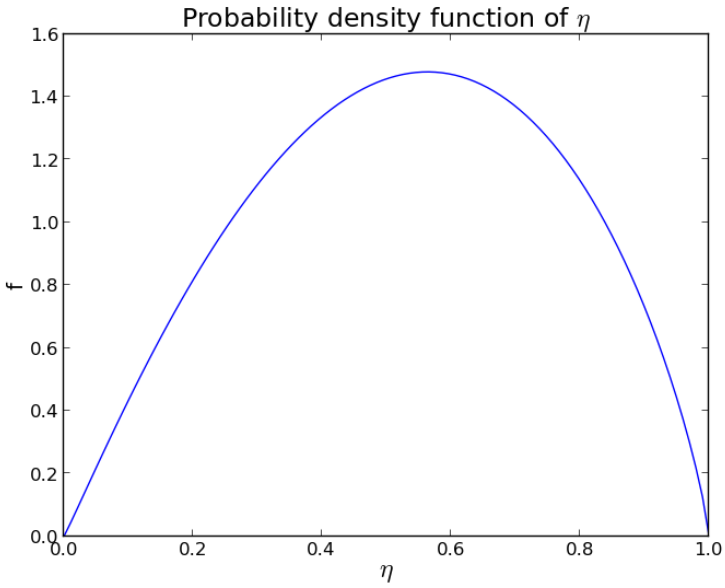

Fig. 2.— The probabilty density function for the distribution of the circularity η from Wetzel (2011), $f(\eta) = 5.3\eta^{1.05}(1-\eta)^{0.813}$.

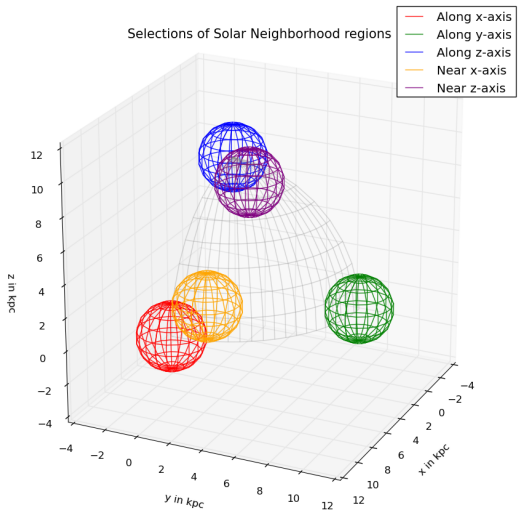

Fig. 3.— The positions of the spherical regions with a radius of 2 kpc resembling the Solar Neighborhood centered on five different locations, namely along the x-axis (8 kpc; 0; 0), the y-axis (0; 8 kpc; 0), the z-axis (0; 0; 8 kpc), near the x-axis (7.48 kpc; 2 kpc; 2 kpc), and near the z-axis (2 kpc; 2 kpc; 7.48 kpc).

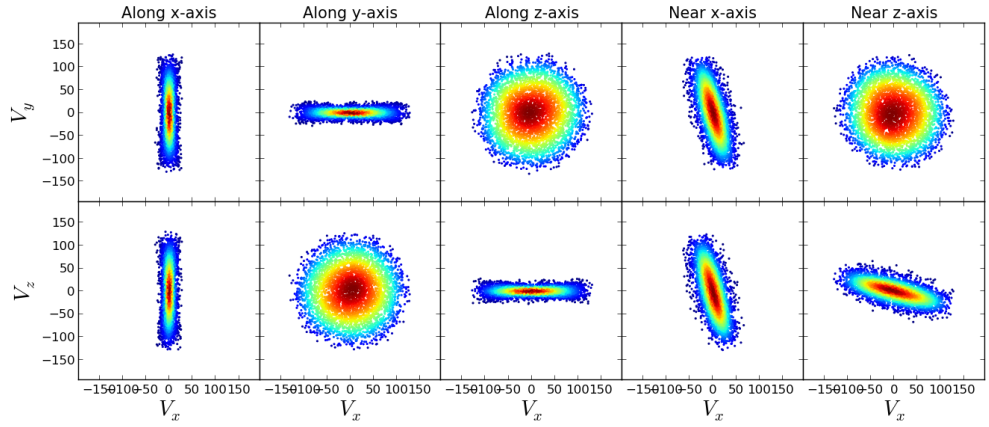

Fig. 4.— The initial velocity distributions in km/s of the particles within the volumes under study of radius 2 kpc located on the x-, y-, and z-axes and near the x- and z-axis. All radial velocities of these stars are zero, so the spread in velocity is expected to be the smallest in the direction that aligns radially with the location of the selections. σ is nowhere zero because the radial direction is not exactly the same for all stars within each volume (54 km/s $> \sigma >$ 8 km/s).

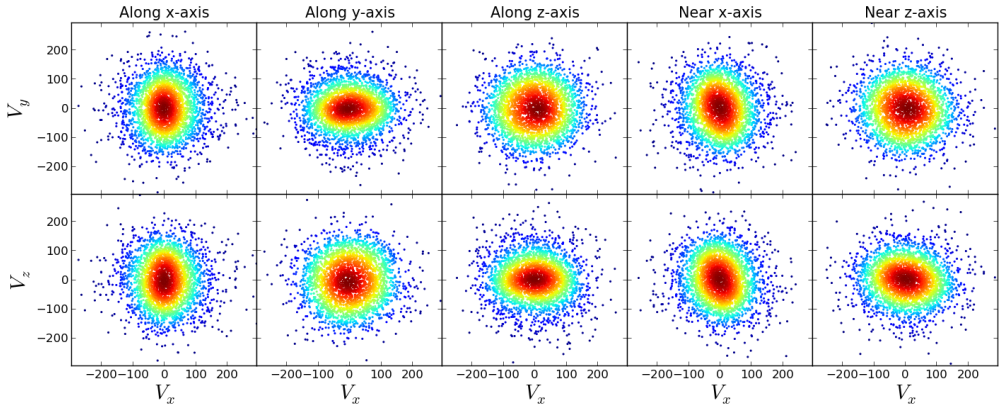

Fig. 5.— The velocity distributions in km/s of the particles within the volumes under study of radius 2 kpc located on the x-, y-, and z-axes and near the x- and z-axis, after integrating them in a spherically symmetric NFW-potential for 8 Gyr. $\bar{V_r} = \bar{V_\theta} = \bar{V_\phi} \sim 0$ km/s, $\sigma_{V_r} \sim 70$ km/s, and $\sigma_{V_\theta} = \sigma_{V_\phi} \sim 80$ km/s.

2.3. The Triaxial NFW Potential

The Aquarius simulations have shown that Milky Way-like dark matter halos are expected to have triaxial mass distributions (Vera-Ciro et al. 2011). By definition, triaxial distributions have three principal axes. This means that the equipotential surface of a triaxial potential has three principal axis sizes, a main axis a, an intermediate axis b, and a minor axis c, by decreasing size. Usually these values are summarized by providing the principal axis ratios b/a and c/a or the triaxiality parameter T which is defined as follows (Binney & Tremaine 2008):

$$T \equiv \frac{a^2 - b^2}{a^2 - c^2} \tag{7}$$

One can see that if $T \sim 0$, then $a \sim b \gg c$, which means that the system is oblate. If $T \sim 1$, then $a \gg b \sim c$, which means that the system is prolate. An interesting value $\tilde{T}$ of the triaxiality of the system occurs when the difference between b and c is exactly equal to the difference between a and b (i.e. no prolate- or oblateness). This is the case when $(b - c) = (a - b)$. When we rewrite this and set a equal to unity, we get $c = 2b - 1$. Since $0 < c < 1$, we know that $0.5 < b < 1$. Inserting the expression for c into Equation (7) with a equal to unity, we get after some algebra an expression for $\tilde{T}$:

$$\tilde{T} \equiv \frac{1 - b^2}{4(b - b^2)} \tag{8}$$

With the limit that $0.5 < b < 1$. Within this range we find that the values of $\tilde{T}$ are in the range $0.5 < \tilde{T} < 0.75$.

Hayashi et al. (2007) showed that the degree of triaxiality in CDM dark matter halos varies with radius, with the potential becoming increasingly spherically symmetric towards larger distances from the halo center. The transition from nonsphericity to sphericity was found to occur on average near the value $r_\alpha \sim 1.2 r_s$, where r_s is the scale radius in the NFW profile. While Hayashi et al. (2007) proposed a modification of the NFW that fits this behavior, Vogelsberger et al. (2007) argued for a different form that lends itself more

easily for deriving the equations of motion which are important for orbital integration. This will be the form used here. These authors have provided a generalisation of the NFW which varies in triaxiality as a function of radius and mirrors the behavior found by Hayashi et al. (2007) qualitatively. Vogelsberger et al. (2007) proposed to replace the radius r from Equation (1) with a more generalized radius-like quantity $\tilde{r}$:

$$\tilde{r} = \frac{(r_\alpha + r)r_E}{(r_\alpha + r_E)} \tag{9}$$

Here r_α is again the transition scale and r_E is a scale that represents the ellipsoidal geometry of the inner region:

$$r_E = \sqrt{\frac{x^2}{a^2} + \frac{y^2}{b^2} + \frac{z^2}{c^2}} \tag{10}$$

Here x, y, and z represent the spatial coordinates along axes that are aligned with, respectively, the major, intermediate, and minor axes. The condition for normalization is that $a^2 + b^2 + c^2 = 3$. This equation is analogous to the generic expression for r:

$$r = \sqrt{x^2 + y^2 + z^2} \tag{11}$$

From Equation (9) we can see that if $r \ll r_\alpha$, $\tilde{r} \cong r_E$, which means that inside the transition radius $\tilde{r}$ is mainly defined by the triaxial radius-like quantity. Conversely, if $r \gg r_\alpha$, $\tilde{r} \cong r$, which means that outside the transition radius $\tilde{r}$ is mainly defined by the spherical radius.

We will consider three sets of axis ratios in our study. Because we are interested in the detectability of triaxiality, one important case would be that of maximal triaxiality that would still be realistic on basis of simulations, for example in the Aquarius simulations under study in Vera-Ciro et al. (2011). Such a degree of triaxiality was used in the paper of Rojas-Niño et al. (2012), in which the axial ratios were $b/a \approx 0.83$, $c/a \approx 0.67$ and the triaxiality parameter $T \approx 0.56$. Therefore we also use these axial ratios. Note here that these are axial ratios for the potential and not for the density distribution which is flatter and has more extreme axial ratios. Recent modelling of the Sagittarius stellar stream (e.g.,

Law & Majewski 2010) has suggested an almost completely oblate dark matter halo with $b/a \approx 0.99$ and $c/a \approx 0.72$ which means that $T \approx 0.04$. Earlier analyses of velocities of stars in the same stellar stream have shown that the shape of the halo might be prolate (Helmi 2004) with $b/a \approx c/a \approx 0.6$ which corresponds with $T \approx 1.0$. These axial ratios were found under different assumptions of the exact form of the potential and fitting different observational sets. Here we will study all three of these parametrizations as summarized in Table 1. For the sake of consistency in each of the three potentials we align each of the major axes with the x-axis, the intermediate axes with the y-axis and the minor axes with the z-axis. Visualizations of their isopotential surfaces are plotted in Figure 6.

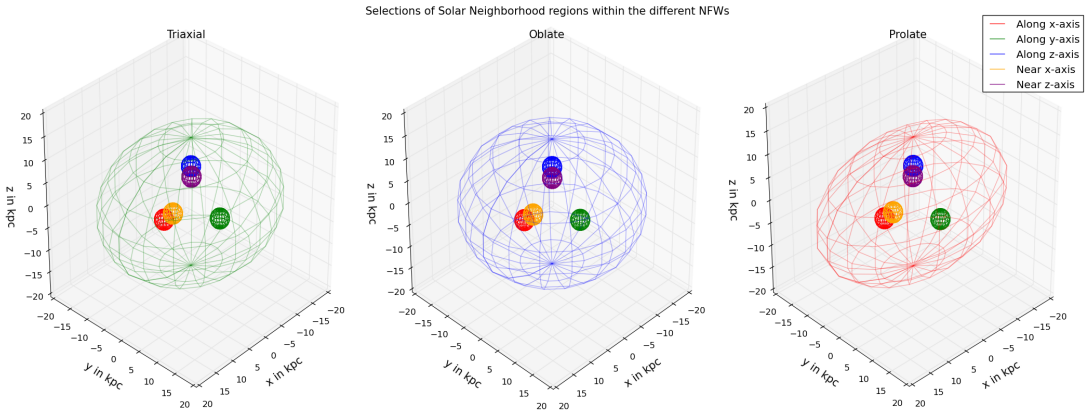

Fig. 6.— Isopotential surfaces for the three different parametrizations (Triaxial, Oblate, Prolate) are visualized here together with the Solar Neighborhood volumes. The major axes are aligned with the x-axis, the intermediate axes with the y-axis and the minor axes with the z-axis.

Table 1: Parametrizations of the different NFW-potentials. The major axes are aligned with the x-axis, the intermediate axes with the y-axis and the minor axes with the z-axis. This means that the oblate potential is almost identical on the x- and y-axes and that the prolate potential is perfectly identical on the y- and z-axes.

	Triaxial	Oblate	Prolate
b/a	0.83	0.99	0.6
c/a	0.67	0.72	0.6

2.4. Derivation of the Equations of Motion

Now that we have a realistic expression for the triaxial NFW potential by combining Equations (1), (9), and (10), we will use that $\vec{g} = -\nabla\Phi$ to find the vector describing the gravitational force $\vec{g}$ that acts upon the test-particles in the potential. Using the chain rule for derivations we arrive at the expressions:

$$\frac{\partial\Phi}{\partial x} = \frac{\mathrm{d}\Phi}{\mathrm{d}\tilde{r}}\frac{\partial\tilde{r}}{\partial x} \tag{12a}$$

$$\frac{\partial\Phi}{\partial y} = \frac{\mathrm{d}\Phi}{\mathrm{d}\tilde{r}}\frac{\partial\tilde{r}}{\partial y} \tag{12b}$$

$$\frac{\partial\Phi}{\partial z} = \frac{\mathrm{d}\Phi}{\mathrm{d}\tilde{r}}\frac{\partial\tilde{r}}{\partial z} \tag{12c}$$

Since the expression $\frac{\mathrm{d}\Phi}{\mathrm{d}\tilde{r}}$ was already derived in Equation (4), we only need to find the partial derivatives of $\tilde{r}$ with respect to the x-, y-, and z-coordinates. Since the shape of the equation is similar with regard to all three of the coordinates, it will be sufficient to only derive the equation with respect to x. Combining the differential product and chain rules to derive Equation (9) with respect to x, we find:

$$\frac{\partial\tilde{r}}{\partial x} = \left(\frac{r_E}{r_\alpha + r_E}\right)\frac{\partial r}{\partial x} + \left(\frac{r_\alpha + r}{r_\alpha + r_E}\right)\left(1 - \frac{r_E}{r_\alpha + r_E}\right)\frac{\partial r_E}{\partial x} \tag{13}$$

Therefore we need the derivatives of r and r_E from Eqs. (11) and (10) with respect to x. After some algebra, we find:

$$\frac{\partial r}{\partial x} = \frac{x}{r} \tag{14}$$

$$\frac{\partial r_E}{\partial x} = \frac{x}{a^2 r_E} \tag{15}$$

These equations hold for y and z if we also replace a by respectively b or c. Then, by combining Eqs. (13), (14), and (15), we can arrive at the partial derivatives of $\tilde{r}$ with respect to x, y, and z:

$$\frac{\partial\tilde{r}}{\partial x} = \frac{x}{r_\alpha + r_E}\left[\frac{r_E}{r} + \frac{1}{a^2}\left(\frac{r_\alpha + r}{r_E} - \frac{r_\alpha + r}{r_\alpha + r_E}\right)\right] \tag{16a}$$

$$\frac{\partial \tilde{r}}{\partial y} = \frac{y}{r_\alpha + r_E}\left[\frac{r_E}{r} + \frac{1}{b^2}\left(\frac{r_\alpha + r}{r_E} - \frac{r_\alpha + r}{r_\alpha + r_E}\right)\right] \tag{16b}$$

$$\frac{\partial \tilde{r}}{\partial z} = \frac{z}{r_\alpha + r_E}\left[\frac{r_E}{r} + \frac{1}{c^2}\left(\frac{r_\alpha + r}{r_E} - \frac{r_\alpha + r}{r_\alpha + r_E}\right)\right] \tag{16c}$$

From this we can obtain the force equations in x, y, and z by multiplying the partial derivatives of $\tilde{r}$ with respect to x, y, and z in Eq. (16) with the derivative of the potential with respect to $\tilde{r}$ in Eq. (4) to find the derivative of the potential with respect to x, y, and z in Eq. (12).

2.5. Leapfrog Integrator

Since the equations of motion have simple analytic forms for our collisionless stellar system, we use the so-called leapfrog or Verlet integrator for our numerical experiments. According to Binney & Tremaine (2008), the leap-frog integrator has multiple advantages. Firstly, it is a second-order integrator but requires essentially the same numerical capacity as first-order approximations. Secondly, it is time reversible which prevents our numerical approximations from drifting away systematically in energy. Thirdly, it does not require saving previous time steps and hence saves memory capacity.

The leap-frog integrator functions best with fixed time steps and for our application we do not need more flexibility than that. In our case the time steps need to be chosen small enough to calculate the precise orbits when stars are at their pericenters, but also as large as possible to avoid wasting numerical capacity when stars are near their apocenters. As the term leapfrog might be interpreted to imply, the algorithm has a specific method of handling time steps Δt in which the changes in spatial and velocity coordinates "jump across each other" in the sense that the particles are allowed to drift for $\Delta t/2$, then they are kicked for Δt, and then again they drift for $\Delta t/2$. Because of this it has also been called "drift-kick-drift" leapfrog, which can be expressed in the following set of equations for the

position vector $\vec{q}$ and the velocity vector $\vec{p}$ as a function of time t, adapted from Binney & Tremaine (2008):

$$\vec{q}\left(t_0 + \frac{\Delta t}{2}\right) = \vec{q}(t_0) + \frac{\Delta t}{2}\vec{p}(t_0) \tag{17a}$$

$$\vec{p}(t_0 + \Delta t) = \vec{p}(t_0) - \Delta t \nabla\Phi\left[\vec{q}\left(t_0 + \frac{\Delta t}{2}\right)\right] \tag{17b}$$

$$\vec{q}(t_0 + \Delta t) = \vec{q}\left(t_0 + \frac{\Delta t}{2}\right) + \frac{\Delta t}{2}\vec{p}(t_0 + \Delta t) \tag{17c}$$

We use these equations to calculate the changes in $\vec{q}$ and $\vec{p}$ per time step Δt. One condition for a particle in a constant potential is conservation of orbital energy. If time steps are taken too big, numerical errors are expected to occur around the pericenters of the orbits (where the changes in the forces are the most extreme), which would then result in a breach of conservation of energy. Therefore we check the conservation of energy along the trajectory of each particle in order to ensure that the time steps Δt were not too big. The orbital energy E at time t is given by:

$$E(t) = \Phi(\vec{q}(t)) + \frac{\vec{p}(t)^2}{2} \tag{18}$$

The condition was that $\Delta E/E_0 < 3{\times}10^{-3}$, which means that the difference between the energy and initial energy is never allowed to become larger than 0.3 percent. We choose a time step for which this condition is valid as Δt, namely 0.1Myr. With this time step, the largest mean deviation from the initial energy is $\overline{\Delta E}/E_0 = 5{\times}10^{-5}$. The positions and velocities are not given as output for each time step, but only as often as strictly necessary to achieve a high enough resolution for our analyses of the orbital characteristics of the particles.

2.6. Kullback-Leibler Divergence

We aim to test the claim by Rojas-Niño et al. (2012) that the presence of orbital resonances causes substructures in the velocity distribution of the stars in the Solar Neighbourhood. Therefore in our numerical experiments we will explore whether there are any significant substructures, i.e. correlations between the velocity coordinates. To this end we will apply the Kullback-Leibler Divergence (hereafter: KLD). We use the KLD to compare a non-correlated distribution $Q(i, j, k)$ of the particles in the three-dimensional cartesian grid (i, j, k) with the distribution $P(i, j, k)$ found in our simulations. For discrete probability distributions in three dimensions we define the KLD-α as:

$$\alpha = \sum_{i,j,k} P(i, j, k) \ln \left(\frac{P(i, j, k)}{Q(i, j, k)} \right) \tag{19}$$

Where $P(i, j, k)$ and $Q(i, j, k)$ are respectively the measured and expected numbers of particles within each bin of the cartesian grid (i, j, k). We loosely tune the bin sizes to the size of the orbital structures based on the orbital analysis that follows below.

In our case, the null hypothesis H_0 is that there is no correlation between V_x, V_y, and V_z. Therefore we have $p_{H_0}(V_x, V_y, V_z) = p(V_x)p(V_y)p(V_z)$, where $p(V_x)$, $p(V_y)$, and $p(V_z)$ are given by:

$$p_i(V_x) = N_i/N_{tot} \qquad p_j(V_y) = N_j/N_{tot} \qquad p_k(V_z) = N_k/N_{tot} \tag{20}$$

Where N_i, N_j, and N_k are the numbers of particles in one-dimensional bins along V_x, V_y, and V_z, respectively. N_{tot} denotes the total number of particles. Then, for all bins denoted by (i,j,k) the expected uncorrelated counts are given by $Q(i, j, k) = p_i p_j p_k N_{tot}$. Subsequently, we generate the distribution of the uncorrelated KLD-α_{H_0} by drawing 3500 times $P(i, j, k)$ from $i \times j \times k$ Poisson distributions with means $Q(i, j, k)$, each time calculating an α_{H_0}-value using Equation (19). An example of a resulting KLD distribution can be found in Figure 7. For each test we also bin the velocities found in the numerical experiment, from which we determine the corresponding experimental value α_{exp} with Equation (19). We evaluate α_{exp}

with the distribution of α_{H_0} which was generated under the assumption of non-correlated velocities, like in Figure 7. Finally, we calculate the probability p of finding α_{H_0} as extreme as or more extreme than α_{exp}, under the null hypothesis. We do this by calculating the accumulative proportion of the α_{H_0}-distribution that falls either on the left of α_{exp} (if $\alpha_{exp} <$ median of the α_{H_0}-distribution), or to the right of α_{exp} (if $\alpha_{exp} >$ median of the α_{H_0}-distribution).

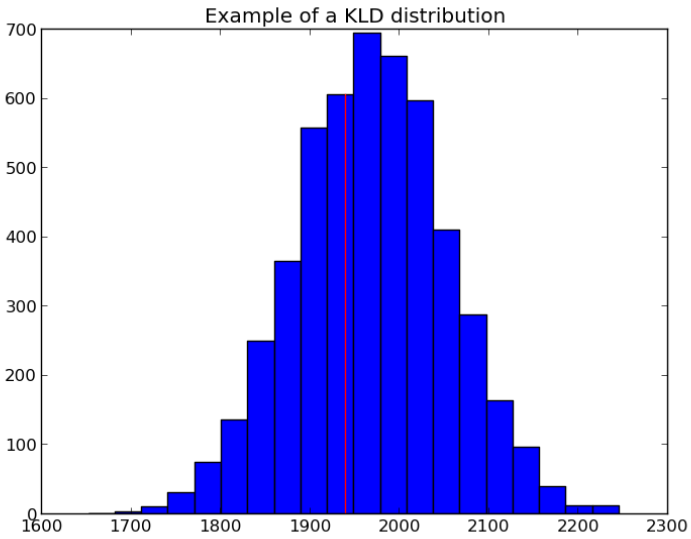

Fig. 7.— A histogram showing the distribution of the value α_{H_0} generated for the case of the selection on the x-axis in the triaxial parametrization (binsize 50 km/s). A possible α_{exp}-value from our numerical experiments is plotted with a red line. The proportion of values α_{H_0} that lie to the left of the red line would be used to calculate the p-value for this example.

2.7. Characterization of Orbital Resonances

In a spherically symmetric potential there is no force gradient in either θ or ϕ and hence all integrated orbits are expected to be confined to planes (see Figure 8). For our initial conditions this consistently resulted in loop orbits, for which the orbits are confined to flat tori around the center. Examples of the trajectories can be seen in Figure 8, where particles from our initial conditions are shown after integration in a spherical NFW and shown both face-on and edge-on. However, inside a triaxial NFW the forces vary both with θ and ϕ and therefore all integrated orbits are expected to probe three-dimensional regions of configuration space. In Figure 9 orbits are shown of particles with the same initial conditions as in Figure 8 but now integrated in a triaxial NFW of the parametrization from Table 1. As is clear from the figure, it is not possible to find a perfect edge-on view of the orbits. These orbits are not all loop orbits like in the case of the spherical potential and they vary in their degree of regularity.

As adapted from Monari et al. (2012), orbits are quasi-periodic when they are regular in an N_d-dimensional space:

$$\vec{q}(t) = \sum_{k=1}^{\infty} \vec{a_k} e^{iF_k t} \tag{21}$$

in which $\vec{q}(t)$ is the vector of the spatial coordinates, $\vec{a_k}$ the vector of the complex amplitudes, and the frequencies F_k are linear combinations of the N_b base frequencies vectorized in $\vec{F_b}$. This means that $F_k = \vec{n_k} \cdot \vec{F_b}$, given that $N_b \leq N_d$. The Fourier transform of an orbit that is quasi-periodic according to this definition will consist of a sum of peaks with amplitudes $\vec{a_k}$. After obtaining the time-series of the orbits through integration, we select the dominant frequencies F_d by taking the frequencies with the highest amplitudes a_k with the spectral orbit classifier of Carpintero & Aguilar (1998). The dimensions we use are x, y, and z for all three potentials. Accordingly, we find three groups of dominant frequencies $\vec{F_{x,d}}$, $\vec{F_{y,d}}$, and $\vec{F_{z,d}}$ for each orbit where we consider a maximum of five per

group. Through a process of subtracting the dominant frequencies and their multiplications from the power spectra and reanalyzing the spectra, the orbit classifier of Carpintero & Aguilar (1998) determines the number N_b of fundamental frequencies F_b that describe the motion of each particle. As seen in Figure 9, most particles in the triaxial potential probe three-dimensional regions of space and therefore most of them are expected to populate either orbits with three base-frequencies, $N_b = 3$, or irregular orbits with $N_b > 3$. More than three base frequencies means that $N_b > N_d$ and such orbits do not fulfill the definition of regularity from Equation (21) which also means that the found frequencies cannot be properly called base frequencies. The so-called 'frequency maps' citepbt08 that are obtained by plotting $F_{2,b}/F_{3,b}$ versus $F_{1,b}/F_{3,b}$ help to visualize the structure in frequency space.

For orbits with $N_b = 3$ that are on a resonance we expect the base frequencies to be coupled in two or three dimensions. We define an orbital resonance as when the ratios of the base frequencies in two or three dimensions of the orbit of a particle is a rational number. This can be expressed by:

$$l_1 F_{1,b} + l_2 F_{2,b} + l_3 F_{3,b} = 0 \tag{22}$$

In which l_1, l_2, and l_3 are integer values and $F_{1,b}$, $F_{2,b}$, and $F_{3,b}$ are the three base frequencies. Particles on orbital resonances follow Equation (22) and should therefore populate straight lines in the frequency map. For examples of such resonance lines in frequency maps, see Figure 13. By fitting the resonance lines with functions of the form $A\frac{F_{1x,b}}{F_{3,b}} + B = \frac{F_{2,b}}{F_{3,b}}$ and imposing the boundary of +/- 0.01, we can specify the integer values l_1, l_2, and l_3 that define each resonance. By combining with Equation (22), we find through simple algebra that the ratios of these values are given by:

$$-\frac{l_1}{l_2} = A \qquad -\frac{l_3}{l_2} = B \tag{23}$$

Which means that $l_1 = -nA$, $l_2 = n$, and $l_3 = -nB$, in which n is the smallest integer value for which l_1, l_2, and l_3 are also integer values.

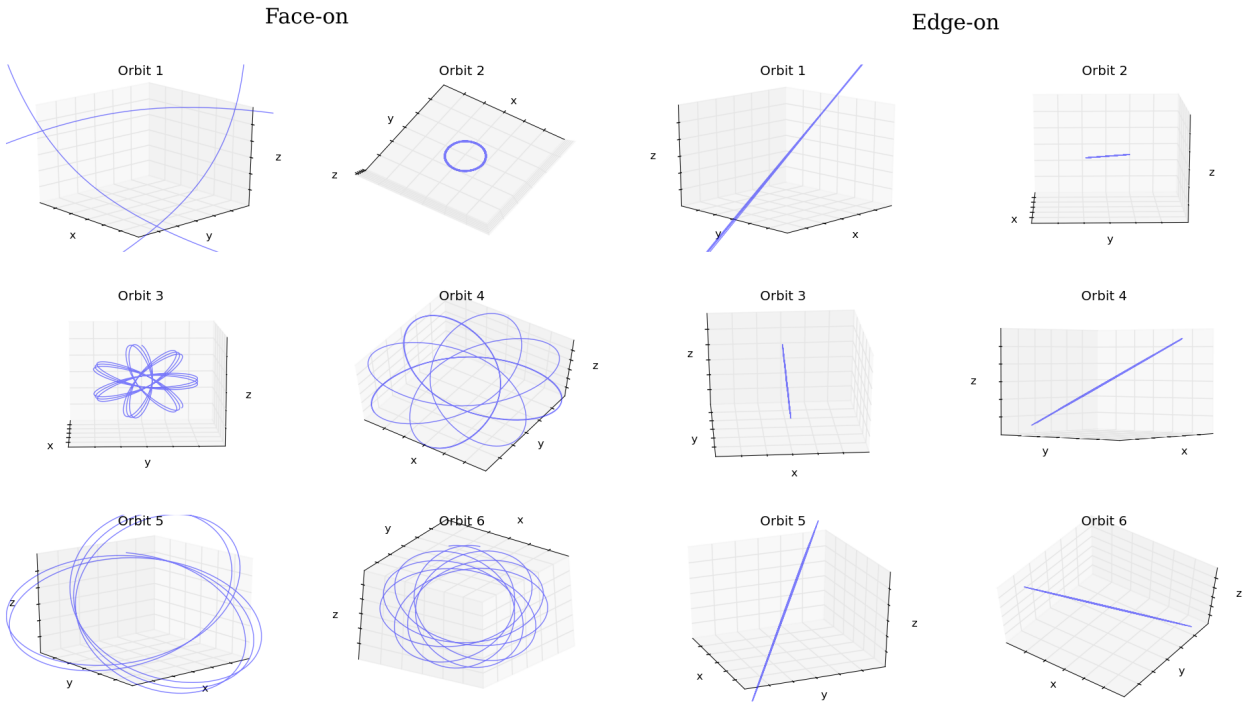

Fig. 8.— Six orbits integrated for 4 Gyr in the spherically symmetric NFW-potential. The orbits are shown both face-on (left) and edge-on (right), to illustrate that all orbits are confined to two-dimensional regions of position space. The axes in all three dimensions range from -15 kpc to 15 kpc.

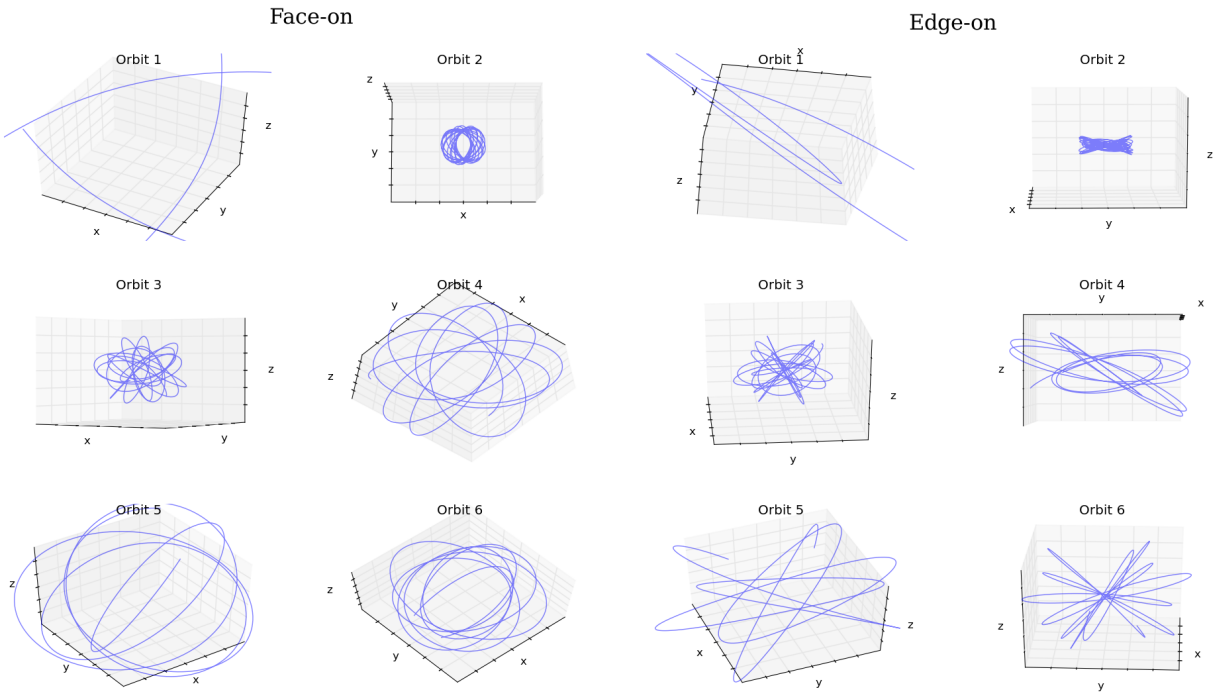

Fig. 9.— Six orbits integrated for 4 Gyr in the triaxial NFW-potential with moderate triaxiality as proposed by Vogelsberger et al. (2007). The initial conditions of the particles were the same as for the previous figure. An attempt has been made to show the orbits face-on (left) and edge-on (right), to illustrate that all orbits now traverse three-dimensional regions of position space. The axes in all three dimensions range from -15 kpc to 15 kpc.

3. Results

3.1. Overall Local Velocity Distributions

We integrate the orbits of two million particles for a duration of 8 Gyr in the potentials of the three shapes, i.e. triaxial, oblate, and prolate (see Figure 6 and Table 1). In Figure 10, we show the resulting velocity distributions within the Solar Neighborhood volumes (SN) located on the three principal axes. Figure 11 shows the distributions for volume close to the major and minor axes. As expected, all mean velocities are found to be ~ 0 km/s. Since the velocity ellipsoids that are located off-axis in the directions of the major and minor axes are somewhat tilted, we rotate them to align with three new axes that we call axis 1, 2, and 3 before we can analyze the velocity distributions. We do this by diagonalizing the covariance matrices of the velocities to determine their eigenvectors (which can be used to rotate the distributions) and their eigenvalues (the squares of the velocity dispersions on the axes 1, 2, and 3). We inspect the velocity distributions after rotation to verify that they are indeed aligned as expected (i.e., not tilted anymore). The dispersions of the velocities are listed in Table 3.1. For the selections in each parametrization the velocity dispersions are the smallest in the radial direction (triaxial, oblate, and prolate: $\sigma_r \sim 67$ km/s). The velocity dispersions are also relatively small in the directions parallel to the major axes (triaxial: $\sigma_{\parallel major} \sim 70$ km/s, oblate: $\sigma_{\parallel major} \sim 75$ km/s, prolate: $\sigma_{\parallel major} \sim 66$ km/s). The velocity dispersions are the largest in the tangential direction and the direction perpendicular to the major axes (triaxial, oblate, prolate: $\sigma_{\perp r, \perp major} \sim 85$ km/s).

The described patterns are a direct indication of the shape of the potential, which could be useful by itself if one would be able to obtain phase-space information of a sufficiently large volume of stars. The set of equations that are relevant to this problem are the Jeans

equations (Binney & Tremaine 2008):

$$\nu \frac{\partial \bar{v_j}}{\partial t} + \nu \bar{v_i} \frac{\partial \bar{v_j}}{\partial x_i} = -\nu \frac{\partial \Phi}{\partial x_j} - \frac{\partial (\nu \sigma_{ij}^2)}{\partial x_i} \tag{24}$$

Here ν is the probability per unit volume of finding a particular star at location $\vec{x}$, Φ denotes the potential, and σ_{ij} denotes the velocity-dispersion tensor. If we assume that the stellar halo is in equilibrium, we have that $\frac{\partial \bar{v_j}}{\partial t} = 0$ for all j. In our setup the term $\bar{v_i} \frac{\partial \bar{v_j}}{\partial x_i} = 0$ for all j because the particles do not a preferred sense of motion. Using this information and applying the product rule for differentiation to the second term on the right of Equation (24), we get:

$$\frac{\partial \Phi}{\partial x_j} = -\frac{\partial (\sigma_{ij}^2)}{\partial x_i} - \sigma_{ij}^2 \frac{\partial \nu}{\nu \partial x_i} \tag{25}$$

in which $\frac{\partial \nu}{\nu \partial x_i}$ is the local proportional variation of the number density of the halo stars across space. Under the assumptions of our setup, measuring this quantity together with the spatial variation in the velocity-dispersion tensor σ_{ij}^2 would give a direct constraint to the form of the potential Φ using Equation (25).

Besides the changes in the overall velocity distributions there did not seem to be any clear substructures when comparing with the distribution in a spherical potential in Fig 5. In the following section, Section 3.2, we present the results regarding the further investigation of these distributions obtained from statistical tests using the KLD method (Section 2.6).

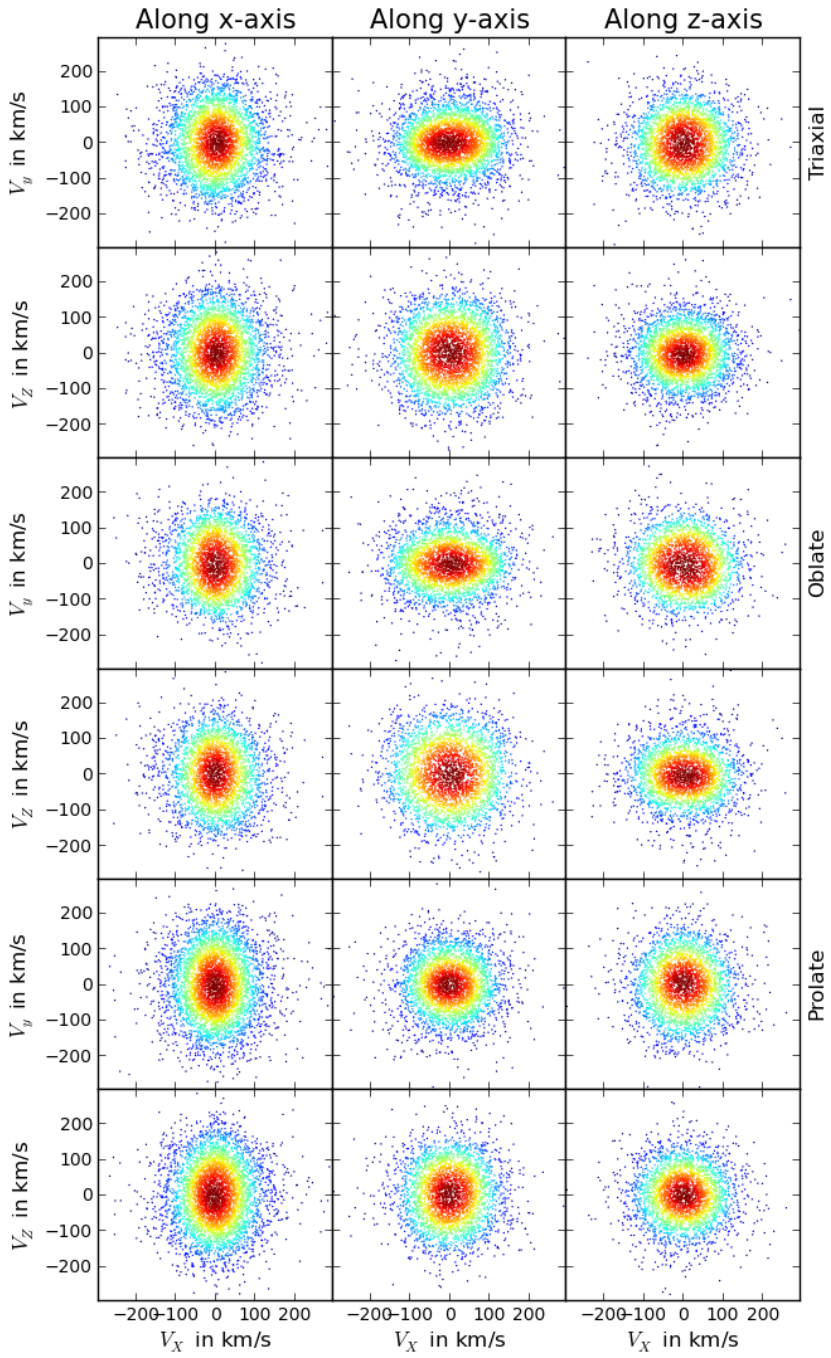

Fig. 10.— Velocity distributions in km/s after integration for 8 Gyr for the triaxial (top two rows), oblate (middle two rows), and prolate (bottom two rows) for the three different locations of the Solar Neighborhood volumes: along the x-, y- and z-axis. Everywhere the major axis is aligned with the x-direction.

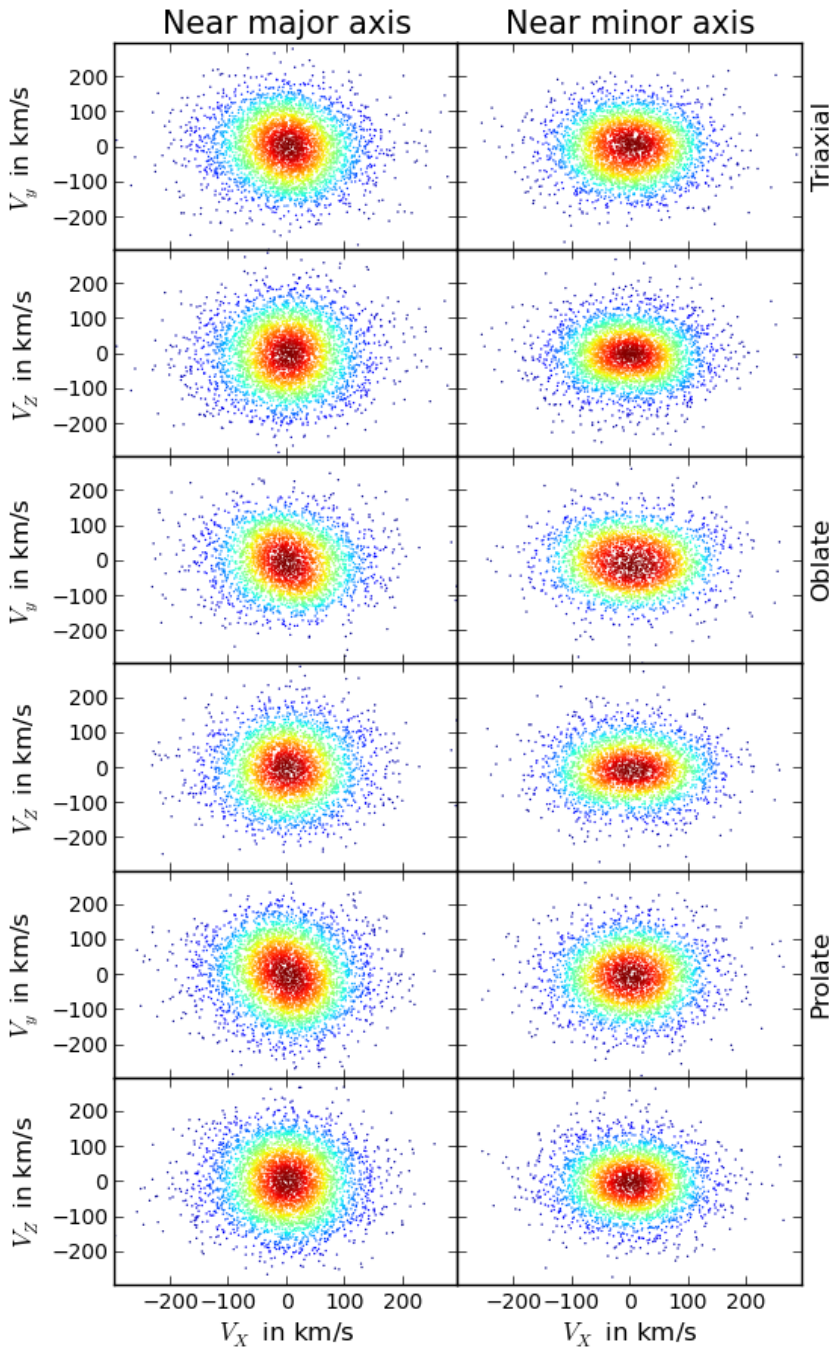

Fig. 11.— Velocity distributions in km/s after integration for 8 Gyr for the triaxial (top two rows), oblate (middle two rows), and prolate (bottom two rows) for the Solar Neighborhood volumes near the x-axis (7.48 kpc; 2 kpc; 2 kpc) and near the z-axis (2 kpc; 2 kpc; 7.48 kpc), $\sim$ 14.7 degrees off-axis. Some distributions are visibily tilted as expected due to the off-axis positioning of the volumes. Everywhere the major axis is aligned with the x-direction.

Table 2: Velocity dispersions in km/s after integration in the volumes considered. For all the on-axis volumes, the velocity ellipsoids are aligned with the x-, y- and z-axes. For the off-axis volumes, the velocity ellipsoids are somewhat tilted. Therefore these are rotated to align with their principal axes. This is reflected in the subscripts of the dispersions.

Triaxial							
	x	y	z			Near Major	Near Minor
σ_x in km/s	68	73	67		σ_1 in km/s	68	65
σ_y in km/s	83	67	74		σ_2 in km/s	86	70
σ_z in km/s	86	82	67		σ_3 in km/s	83	74
Oblate							
	x	y	z			Near Major	Near Minor
σ_x in km/s	66	78	71		σ_1 in km/s	66	66
σ_y in km/s	79	66	71		σ_2 in km/s	79	73
σ_z in km/s	83	85	67		σ_3 in km/s	84	72
Prolate							
	x	y	z			Near Major	Near Minor
σ_x in km/s	64	67	66		σ_1 in km/s	66	77
σ_y in km/s	89	71	79		σ_2 in km/s	86	67
σ_z in km/s	88	79	71		σ_3 in km/s	89	70

3.2. Statistical Tests on Local Velocity Distributions

We apply the KLD as described in Section 2.6 to determine the amount of substructure in the velocity distribution. We use three different binning sizes, 25 km/s, 50 km/s, and 100 km/s. The binning sizes of 50 km/s and 100 km/s are plotted in Figure 12. The ranges of the tests are set to span the full ranges of the velocity distributions from the previous section. For the off-axis selections, we use the same rotations of the velocity distributions as described in Section 3.1 to align with the principal axes of the velocity ellipsoids. Our null hypothesis H_0 is that there are no correlations between the velocities across the different dimensions. Since there are three different binning sizes and five different volumes for three different shapes of the potential, we perform a total of 45 statistical tests. For each of these tests, we perform the following procedure (more details in Section 2.6).

The null hypothesis H_0 determines the expected velocity distribution for a particular test. With that distribution we randomly generate 3500 velocity distributions. Using Equation (19), we find 3500 values for α_{H_0} using the non-correlated distributions and we find one value α_{exp} using the original velocity distribution of the respective test. We then compare α_{exp} with the distribution of α_{H_0} by calculating the proportion of α_{H_0}-values that are more extreme than α_{exp} (e.g., the proportion of values to the left of the red line in Figure 7). This is the estimated probability p_{exp} of finding a value α_{H_0} more extreme than α_{exp}, given that the null hypothesis H_0 is true. We consider a departure from the null hypothesis to be significant when $p_{exp} < p_{cutoff}$. We choose the cutoff probability $p_{cutoff} = 0.00003$ which is the equivalent of a departure of 4σ from the mean of a normal distribution.

The results of this procedure are listed in Table 3.2. There is variation in the p_{exp}-values within the range of 0.07-0.50, therefore $p_{exp} \gg p_{cutoff}$ for all 45 tests. We conclude that all of the velocity distributions from our numerical experiments do not deviate significantly from the corresponding non-correlated velocity distributions.

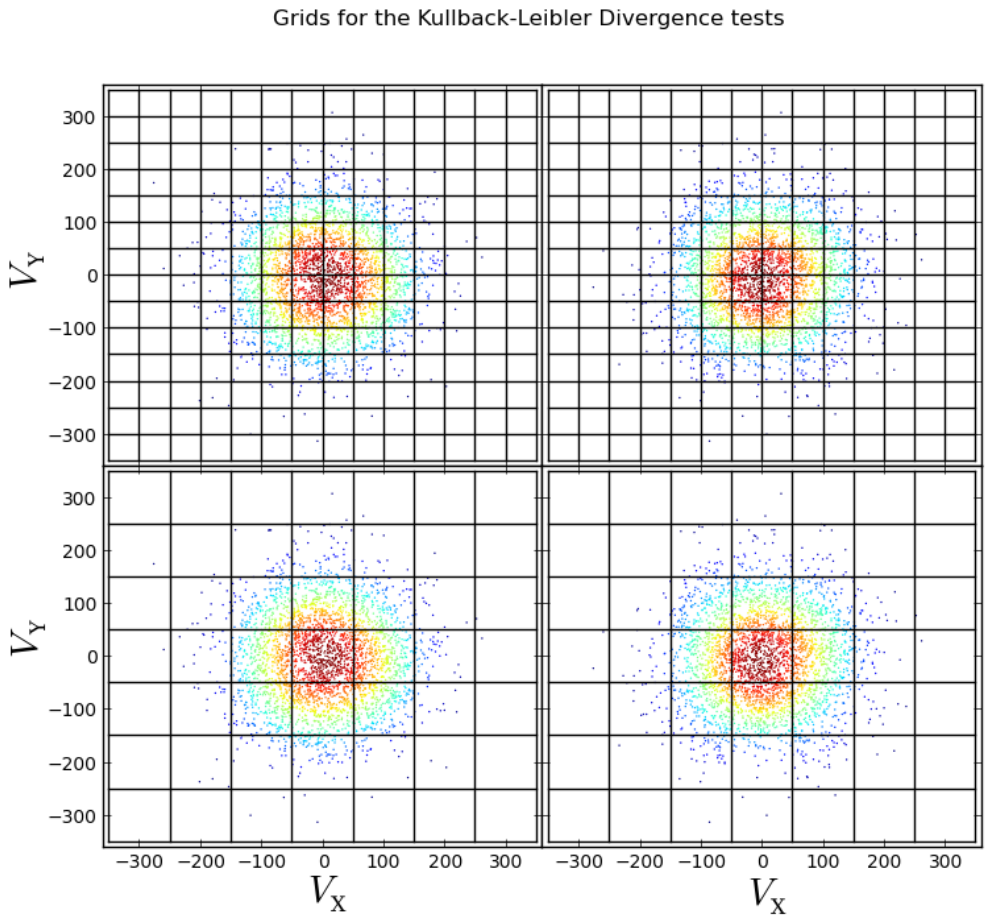

Fig. 12.— The grids for the KLD method with scales 50 km/s and 100 km/s. On the left is the velocity distribution in km/s on the y-axis in the oblate potential and on the right a version in which V_Y was randomly shuffled.

Table 3: Summary of the outcome of the statistical analyses using the KLD method with binsizes of 25 km/s, 50 km/s, and 100 km/s. These values are the estimated probabilities of obtaining the data of our simulations under the null hypothesis that there are no correlations between the velocities across the different dimensions.

25 km/s		x	y	z	Near Major	Near Minor
	triaxial	0.27	0.27	0.18	0.21	0.19
	oblate	0.36	0.31	0.29	0.48	0.40
	prolate	0.47	0.07	0.38	0.47	0.36
50 km/s		x	y	z	Near Major	Near Minor
	triaxial	0.41	0.12	0.22	0.37	0.15
	oblate	0.34	0.28	0.25	0.24	0.29
	prolate	0.41	0.19	0.47	0.36	0.37
100 km/s		x	y	z	Near Major	Near Minor
	triaxial	0.47	0.28	0.43	0.45	0.34
	oblate	0.50	0.41	0.39	0.46	0.48
	prolate	0.44	0.37	0.42	0.47	0.47

3.3. Resonance Populations Identified with Fourier Analysis

After integrating the two million particles for 8 Gyr in the three potentials we select the particles from the volumes indicated in Figure 3. This results in 15 selections in total with about three-thousand particles per volume. Subsequently, we analyze the orbits of these particles in Fourier space using the orbit classifier of Carpintero & Aguilar (1998). To this end it is necessary that we integrate these particles again but for a very long time to ensure that the Fourier analysis can be performed adequately. This means in practice that the orbits should make at least 80 revolutions around the center of the halo ($\sim$ 66 Gyr).

The results of this analysis are shown in Figure 13 where we plot the frequencies against each other: $F_{1,b}/F_{3,b}$ versus $F_{2,b}/F_{3,b}$ in all three potentials. We use Equation (22) to identify the particles that populate resonances and the different types of resonances, with the condition that the particles should be within a range of +/- 0.01 of a resonance line. The fractional distributions of the orbits over the resonances in each potential are reported in Table 3.3.

We also use the orbit classifier of Carpintero & Aguilar (1998) to determine which fractions of the orbits are irregular. According to the definition used here, an orbit is irregular when it seems to have more than three base frequencies in three dimensions (which means that these are not real base frequencies). The results of this analysis are listed in Table 3.3.

In Table 3.3, we see that on and near the major axis (x) in the triaxial potential a relatively large fraction of the particles populates resonant orbits ($\sim$ 20 percent). About half of these particles are on orbits that are coupled in three dimensions, they populate the resonances (l_1:l_2:l_3) = (3:1:6),(1:2:6), and (3:4:24). The other halve of the resonant orbits are coupled in only two dimensions. On the intermediate and minor axes we see a much smaller fraction of resonant orbits ($\sim$ 5 percent).

Regarding the oblate potential, Table 3.3 shows that on the major (x) and intermediate (y) axes fractions of about 12-15 percent of the particles populate resonant orbits, while it is only around one percent on the minor axis (z). All the particles on resonant orbits are coupled in only two dimensions, except for a negligible fraction (0.1-0.2 percent) near the major and minor axes that populates (l_1:l_2:l_3)= (3:1:6).

Regarding the prolate potential, Table 3.3 shows that on the major axis (x) a fraction of $\sim$ 10 percent of the particles populates resonant orbits, while it is only 2.5 percent on the two minor axes (y and z). All the particles on resonant orbits from all selections are coupled in only two dimensions. On the two minor axes, in total just a few percent of the orbits are resonant. Generally, in all three potentials there is a small fraction (a few percent) of so-called thin orbits, which only have two base frequencies. For the selections near the major and minor axes the fractional distributions are generally very similar to the selections on those respective axes.

Table 3.3 summarizes the overall findings regarding the fractional distribution of the irregular orbits, non-resonant regular orbits, the resonant orbits (coupled in two or three dimensions) and the thin orbits. We see that in the volumes on the major axes of the potentials there are consistently larger fractions of irregular orbits as compared with the minor axes. The contrast is the strongest in the triaxial potential (7 percent versus 25 percent).

In summary, we note that in each volume the fractions of resonant orbits and irregular orbits are small compared to the fraction of non-resonant regular orbits. The exception is on and near the major axis of the triaxial potental where there are relatively large fractions of both resonant and irregular orbits. Only in the triaxial potential we find a notable fraction of resonant orbits that are coupled in three dimensions.

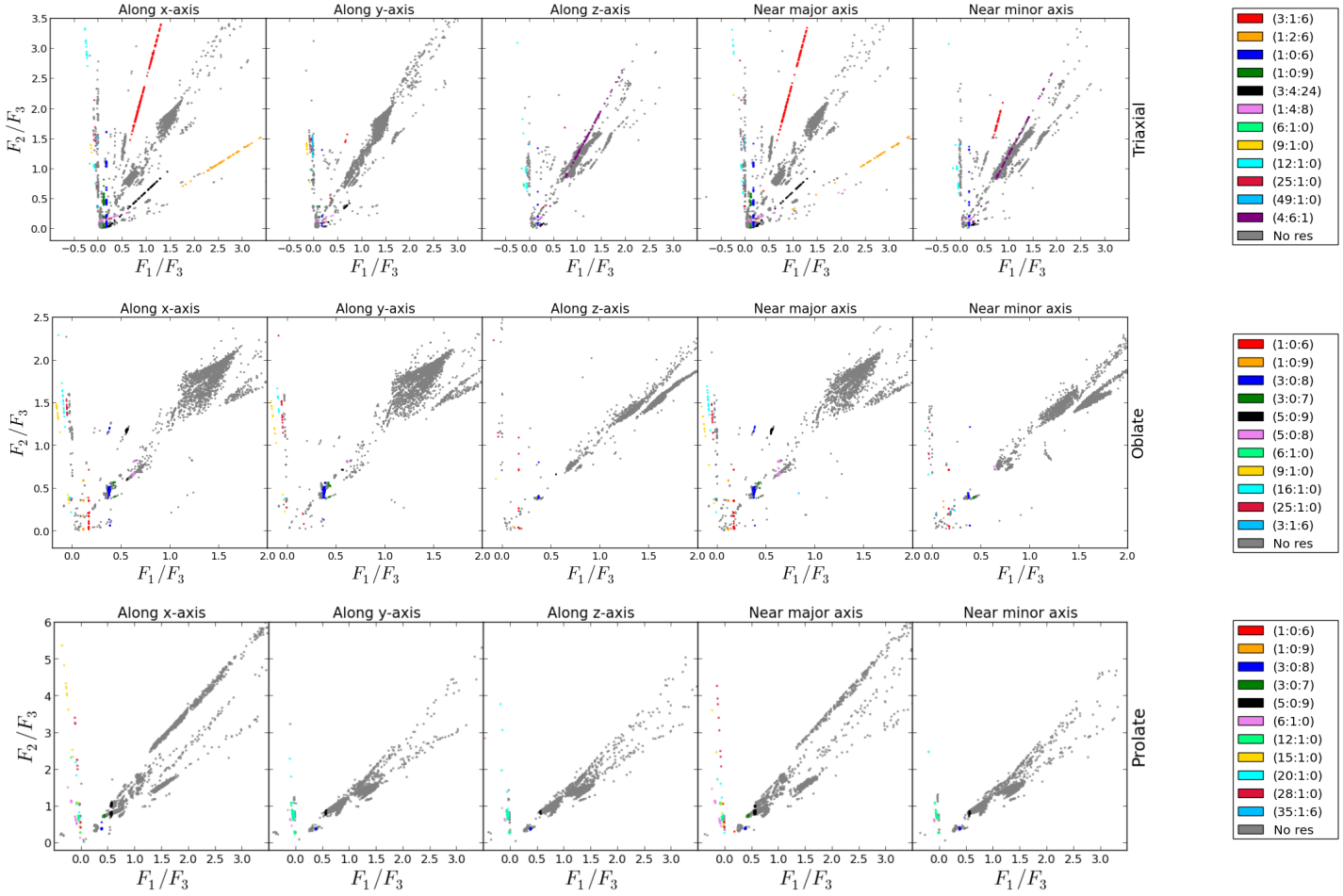

Fig. 13.— Frequency space of about three-thousand orbits that were integrated within a triaxial NFW according to Rojas-Niño et al. (2012) (top row), within an oblate NFW (middle row), and within a prolate NFW (bottom row). Selections consist of volumes of radius 2 kpc located on the x-, y-, and z-axes and near the major and minor axes. Orbital resonances are distinguished by lines that follow the equation $l_1 F_{1,b} + l_2 F_{2,b} + l_3 F_{3,b} = 0$ with all l integer numbers and $\vec{F_b}$ the three base frequencies. The selection criterion for a particle to belong to a resonance is that its distance to a resonance line should not be larger than 0.01 in frequency space.

Table 4: The fractional distribution of the orbits over the populations of resonant orbits in $(l_1 : l_2 : l_3)$, non-resonant orbits, and thin orbits (orbits with only two base frequencies) for the triaxial, oblate, and prolate potentials.

Triaxial	red	orange	blue	green	black	violet	springgreen	gold	cyan	crimson	deepskyblue	purple	grey	yellow
	(3:1:6)	(1:2:6)	(1:0:6)	(1:0:9)	(3:4:24)	(1:4:8)	(6:1:0)	(9:1:0)	(12:1:0)	(25:1:0)	(49:1:0)	(4:6:1)	No res	Thin
x (%)	4.3	2.3	**6.6**	2.2	1.1	1.8		0.1	0.6	0.2	0.2		**78.9**	1.6
y (%)	0.1		0.3	0.1	0.4	0.3		0.4		0.3	0.6		**95.4**	2.0
z (%)	0.1		0.4		0.2	0.2	0.2	0.0	0.4			3.0	**94.7**	0.8
Near Major (%)	3.9	1.9	**5.7**	1.6	1.1	1.8			0.4	0.1	0.1		**81.8**	1.3
Near Minor (%)	1.3		1.1		0.2	0.3			0.6		0.1	2.9	**92.9**	0.6
Oblate	red	orange	blue	green	black	violet	gold	cyan	crimson	deepskyblue			grey	
	(1:0:6)	(1:0:9)	(3:0:8)	(3:0:7)	(5:0:9)	(5:0:8)	(9:1:0)	(16:1:0)	(25:1:0)	(3:1:6)			No res	2 base
x (%)	1.3	1.0	**5.3**	0.4	1.0	1.0	0.7	0.6	0.3				**85.4**	3.1
y (%)	0.1		**5.3**	0.3	0.0	0.1	0.5	0.5	0.5				**88.8**	3.9
z (%)	0.3		0.3						0.1				**98.4**	0.8
Near Major (%)	1.3	0.8	**5.2**	0.2	1.0	1.4	0.5	1.0	0.6	0.1			**85.0**	3.1
Near Minor (%)	0.4	0.1	0.6	0.2		0.0		0.1	0.1	0.2			**96.4**	1.8
Prolate	blue	green	black	violet	springgreen	gold	cyan	crimson					grey	
	(3:0:8)	(3:0:7)	(5:0:9)	(6:1:0)	(12:1:0)	(15:1:0)	(20:1:0)	(28:1:0)					No res	2 base
x (%)	1.0	1.8	3.6	1.7	0.5	0.6	0.2	0.3					**88.1**	2.1
y (%)	0.5		0.4	0.2	1.0		0.3						**94.6**	2.9
z (%)	0.6		0.2	0.3	0.9		0.4						**94.1**	3.4
Near Major (%)	1.2	1.5	4.4	1.1	0.6	0.4	0.2	0.6					**87.7**	2.3
Near Minor (%)	0.6		0.4	0.3	0.9		0.1						**94.1**	3.5

Table 5: The fractional distribution of non-resonant orbits (regular and irregular), resonant orbits (coupled in two or three dimensions) and thin orbits on the x-, y-, and z-axes and near the major and minor axes in the triaxial, oblate, and prolate potentials. The x-, y- and z-axes are consistently aligned with the major, intermediate and minor axes of the potentials.

Triaxial		x	y	z	Near Major	Near Minor
Non-resonant	Regular (%)	53.8	90.5	88.1	58.8	85.1
	Irregular (%)	25.1	4.9	6.6	23.0	7.8
Resonant	2D-coupled (%)	10.0	1.8	1.0	8.2	1.8
	3D-coupled (%)	9.5	0.8	3.5	8.7	4.7
Thin (%)		1.6	2.0	0.8	1.3	0.6

Oblate		x	y	z	Near Major	Near Minor
Non-resonant	Regular (%)	73.9	80.9	97.0	75.5	94.1
	Irregular (%)	11.5	7.9	1.4	9.5	2.3
Resonant	2D-coupled (%)	11.5	7.3	0.8	11.8	1.6
	3D-coupled (%)				0.1	0.2
Thin (%)		3.1	3.9	0.8	3.1	1.8

Prolate		x	y	z	Near Major	Near Minor
Non-resonant	Regular (%)	84.4	93.5	93.0	84.8	92.5
	Irregular (%)	3.7	1.1	1.1	2.9	1.6
Resonant	2D-coupled (%)	11.9	5.4	5.9	12.3	5.9
Thin (%)		2.1	2.9	3.4	2.3	3.5

3.4. Resonance Populations in Velocity Space

Now we link the information of the resonance groups from Section 3.3 back to the velocity distributions of the particles for the selected volumes on the axes. The resonance populations identified in frequency space are shown in velocity space in Figure 14 for the triaxial potential and in Figure 15 for the oblate and prolate potentials. For the triaxial potential we see that on and near the major axis x different resonances populate different cylindrical shells in velocity space, all varying in their orientation. For example, the resonance $(l_1{:}l_2{:}l_3) = (1{:}2{:}6)$ forms a small well-defined ring at $|V_{x,z}| \sim 50$ km/s in the bottom left plot of Figure 14, while the resonance (3:1:6) forms two walls which have the range of +/- 150 km/s in V_x and V_z which center on $V_y = 50$ km/s and -50 km/s. The particles on thin orbits populate mainly the regions of $|V_y| > 100$ km/s. On the y- and z-axes much smaller fractions of the particles populate resonances and the patterns are not as pronounced as on the x-axis. Nevertheless, some features can be distinguished. For example, the resonance (3:4:24) forms a narrow line at $V_x = V_z = 0$ km/s on the y-axis and particles from the resonance (4:6:1) mostly populate a bar-shaped region of thickness 50 km/s centered on $V_x = 0$ km/s.

For the oblate potential we also see patterns in the velocities of the particles from the different resonance populations, especially on the x-axis. For example, the resonances $(l_1{:}l_2{:}l_3) = (1{:}0{:}6)$, (1:0:9), (5:0:9), (5:0:8) form a slice in the region $|V_y| \sim 25$ km/s on the x-axis. This appears to be caused by the slight difference in the potential between the major and intermediate axes, because the same structure is not visible on the y-axis. On both of these axes, the resonances (6:1:0) and (3:0:8) populate similar regions in velocity space as the thin orbits, while on the x-axis they have $|V_y| > 50$ km/s and on the y-axis they have $|V_x| > 50$ km/s. while in V_x this resonance covers only the range of +/- 50 km/s. On the minor axis z there are to few particles on resonant orbits to say something concrete about

their distribution, although they do not seem to follow the overall distribution of particles.

For the prolate potential, the main pattern on the major axis x consists of cylindrical shells aligned with V_x. For example, the resonance (l_1:l_2:l_3) = (5:0:9) populates both an inner region of $|V_{y,z}| < 50$ km/s and a well-defined, thin cylindrical shell at $|V_{y,z}| \sim 100$ km/s. Within the range $75\ km/s > |V_{y,z}| > 150$ km/s, the resonances (6:1:0), (3:0:7), (3:0:8), (12:0:1), and (28:1:0) form additional cylindrical shells. The only pattern visible on the minor axes is that of the resonance (3:0:8), although it is not very pronounced because the fraction of particles that populate it is very small.

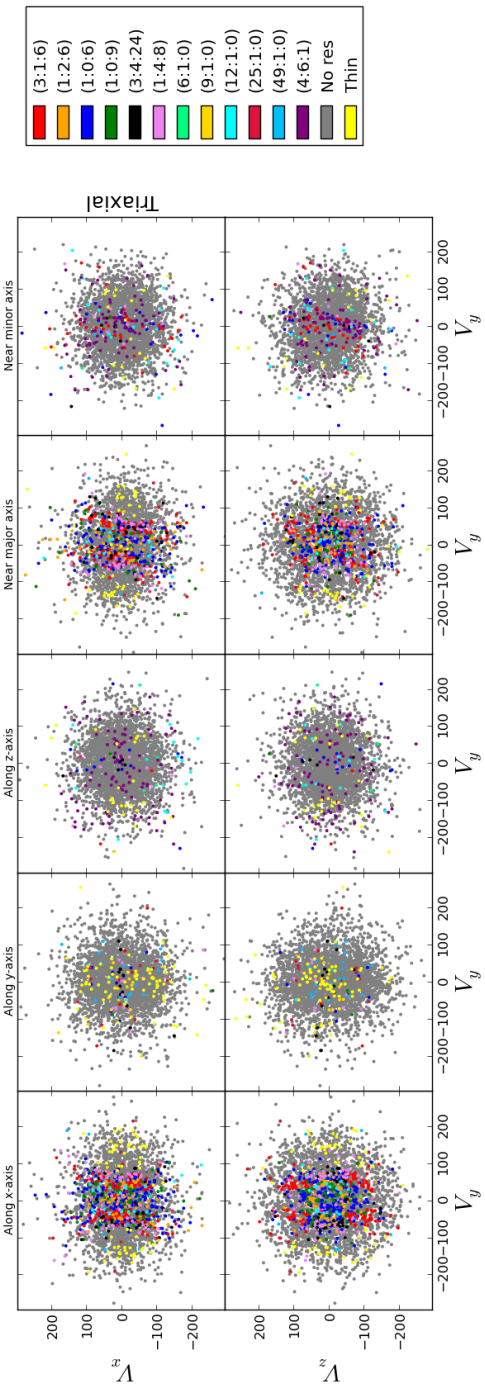

Fig. 14.— The velocity distributions in km/s of the selections along the x, y, and z-axes and near the major and minor axes after integrating within the triaxial NFW. Orbital resonances selected from Figure 13 are represented by the different colors. Clearly particles on resonances occupy specific regions of velocity space.

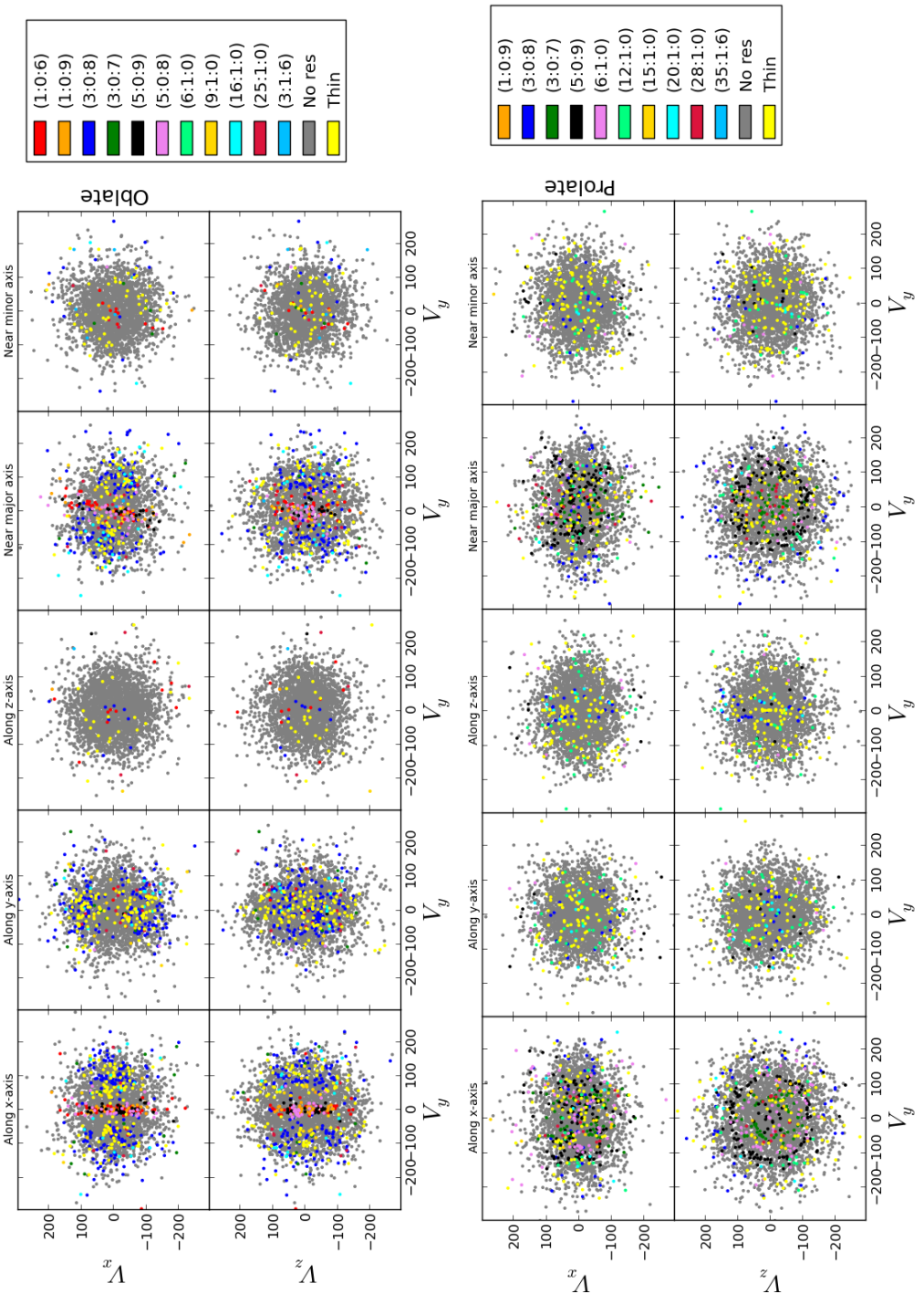

Fig. 15.— Same as in Figure 14 but now for the oblate and prolate cases.

4. Discussion

We conducted numerical experiments with test particles in a Milky Way-like dark matter halo of three different shapes: triaxial, oblate, and prolate. We generated initial conditions for these test particles following a smooth distribution function. The goal was to investigate the assertion of Rojas-Niño et al. (2012) that orbital resonances caused by the shape of the halo would leave imprints in velocity space of the Solar Neighborhood. After our simulations the particles within different SN volumes were studied in more detail. Firstly, we conclude that the only directly observable kinematic differences compared to a spherical dark matter halo were found in the overall shape of the velocity ellipsoids of particles. More specifically, the velocity dispersions of particles within the volumes depended on the locations of the volumes with respect to the axes of the potential and on the shape of the potential itself. Secondly, while resonances were indeed present and related to specific regions in velocity space, they were not well populated. Lastly, we found that the velocity distributions within the Solar Neighborhood volumes did not show any significant substructures for any of the three potentials. Therefore, our numerical experiments show that a smooth initial distribution of particles does not favor any particular orbital resonance that can clearly differentiate the three shapes from each other or from the spherical case.

The second part of our conclusion is in agreement with the findings of Rojas-Niño et al. (2012), namely that certain regions in the velocity distribution of particles in the Solar Neighborhood are related to certain resonances defined by the geometry of the dark matter halo. However, our findings do not support the main claim of these authors that orbital resonances are imprinted on the kinematics and could be used for constraining the shape of the Milky Way dark matter halo. The difference in results can be explained by inspecting the method of these authors in light of our results.

The most significant feature of the method of Rojas-Niño et al. (2012) here is that it

selected only those particles that would return to the same volume of radius 1 kpc after 12 Gyr. There are two effects of this selection that are relevant. Firstly, it is clear that it selectively eliminates most of the particles that do not populate any resonance, since those are less likely to return to the same volume. This is important because in our simulations the non-resonant particles seemed to fill the gaps between the resonance populations in the velocity distributions.

Secondly, the method also seems to select only a subgroup of all the resonance populations. The orbital structure found in our simulations with a complete stellar halo showed resonance populations that were not clearly present in the final selections from the simulations of Rojas-Niño et al. (2012). When we compare the top left plot from Figure 14 from our study with the corresponding figure from their paper (bottom plot of Figure 3 from Rojas-Niño et al. 2012), we see for example that the resonance $(l_1{:}l_2{:}l_3) = (1{:}0{:}6)$ is not present in their selection. One reason for this could be that this resonance is only coupled in two of the three dimensions which might cause the particles from this population to return less often to the same volume defined in x, y, and z as compared to particles that populate resonances coupled in three dimensions. To explore this interpretation of the results we reproduced our results while selecting only the resonances that were coupled in three dimensions. The resulting velocity distribution from Figure 16 indeed contained a pattern similar to that found by Rojas-Niño et al. (2012), even though the volume from which we select here is somewhat larger than theirs (radius 1.5 kpc instead of 1 kpc).

As stated in the introduction, Monari et al. (2012) conducted numerical experiments to study the kinematic effects of the Galactic bar on the stars of the Galactic disc. The findings of these authors did show substructures in the velocity space of the local disk stars that could be useful for constraining the exact shape and orientation of the Galactic bar. We might ask why there would be significant substructures in the velocity distributions of

the disk stars caused by the Galactic bar, but not in those of the halo stars caused by the triaxiality of the Galactic halo. The most important difference with our study is probably that the Galactic disc and the bar have a strong rotation themselves, so the disc particles already have a strong preferred sense of motion. Hence there is little variation in the orbital families that result from resonances with the Galactic bar. This subsequently makes them more pronounced and easier to identify in velocity space. In contrast with this, the halo stars do not have a strong preferred sense of motion.

Our simulations showed that for a stellar halo that follows a smooth distribution function it is unlikely that any orbital resonance would be overpopulated in such a way that it would cause significant overdensities in the corresponding regions of velocity space. However, it is also known that the number of 'building blocks' of the Milky Way's inner and outer stellar halos is probably relatively small (e.g., Morrison et al. 2009; Deason et al. 2015). The traces of these accretion events are expected to be visible through substructures in velocity space (e.g., Helmi 2008). Future simulations could be used to focus on the development of substructures in the stellar halo formed by relatively few progenitors in triaxial, oblate, and prolate potentials. There would be substructures which depend strongly on the infall parameters of the building blocks and which subsequently decrease in spatial density over a certain duration of time as the particles diffuse away. This diffusion timescale varies with the regularity of the progenitor orbit since particles on irregular orbits diffuse away more quickly (Martin Mestre, priv. comm.). Therefore, if within a certain volume of space large fractions of the orbits are irregular, we expect within that volume to see denser spatial substructures belonging to the resonant regions of velocity space than to the non-resonant regions. To investigate this, we also analyzed the fractions of regular orbits in the non-resonant population.

Our analysis of the irregularity of the orbits showed that the fraction of irregular orbits

is only relatively large in the volumes located near the major axis in the triaxial potential. Therefore, under the assumptions that we made in setting up the initial conditions and the potential, the effects of chaotic diffusion of stream particles are largely limited to the major axis. In that case, an analysis would not give any definitive information before we can carry it out on multiple volumes on entirely different locations within the potential (to ensure that the major axis is included). With so much information it might be much simpler just to analyze the velocity dispersions as we will discuss shortly. Note that we cannot say whether this restriction is general enough to extend beyond our chosen setup of initial conditions and potential. In reality there might be larger fractions of irregular orbits. Due to the lack of accurate and extensive data very few substructures in velocity space of local halo stars have been detected thus far (as summarized by Helmi 2008). This information will come within our reach within the coming two years with the upcoming data from the Gaia project (Perryman et al. 2001).

The only observable differences that we found were in the overall shape of the velocity ellipsoids. This means that if we would have six-dimensional phase-space information of most of the stars within a large region (e.g. ~ 6 kpc radius around the Sun), this information could be used to pin down the shape of the potential of the dark matter halo. Data that might help in this respect will also be made available by the Gaia project (Perryman et al. 2001). For example, it will measure the radial velocities at 10 km/s accuracy of stars down to magnitudes of $V \sim 16 - 17$. Since the method proposed by Rojas-Niño et al. (2012) of constraining the halo shape through orbital resonances of nearby stars does not seem to be feasible as shown by our simulations, we conclude that the most promising way to deduce information about the shape of the Galactic dark matter halo from the kinematics of halo stars would be to inspect the changes in the velocity ellipsoids across space.

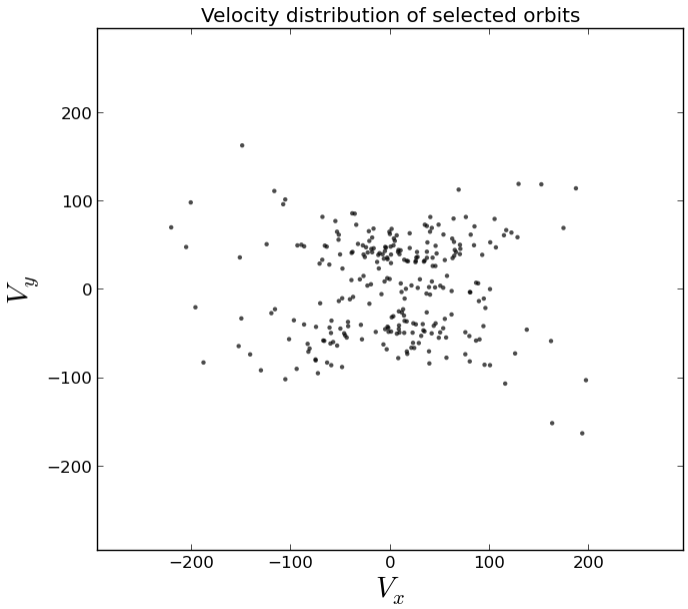

Fig. 16.— The velocity distribution in km/s of the particles from the Solar Neighborhood volume of radius 1.5 kpc located 8.5 kpc from the center on the x-axis after selecting only the particles that populate the resonances (l_1:l_2:l_3) = (3:1:6), (1:2:6), and (1:4:8) because these might be expected to have been overselected in the study of Rojas-Niño et al. (2012). Comparison with Figure 3 from the paper of these authors indeed shows correspondence, even though their selection volume is somewhat different in terms of size (radius 1 kpc).

REFERENCES

Allgood, B., Flores, R. A., Primack, J. R., et al. 2006, MNRAS, 367, 1781

Battaglia, G., Helmi, A., Morrison, H., et al. 2006, MNRAS, 370, 1055

Binney, J., & Tremaine, S. 2008, Galactic Dynamics: Second Edition, by James Binney and Scott Tremaine. ISBN978-0-691-13026-2 (HB). Published by Princeton University Press, Princeton, NJ USA, 2008.,

Busha, M. T., Marshall, P. J., Wechsler, R. H., Klypin, A., & Primack, J. 2011, ApJ, 743, 40

Carpintero, D. D., & Aguilar, L. A. 1998, MNRAS, 298, 1

Cautun, M., Frenk, C. S., van de Weygaert, R., Hellwing, W. A., & Jones, B. J. T. 2014, MNRAS, 445, 2049

Cole, S., Lacey, C. G., Baugh, C. M., & Frenk, C. S. 2000, MNRAS, 319, 168

Deason, A. J., Belokurov, V., & Weisz, D. R. 2015, arXiv:1501.02806

Hayashi, E., Navarro, J. F., & Springel, V. 2007, MNRAS, 377, 50

Hayashi, E., & White, S. D. M. 2008, MNRAS, 388, 2

Helmi, A. 2004, ApJ, 610, L97

Helmi, A. 2008, A&A Rev., 15, 145

Ibata, R., Lewis, G. F., Martin, N. F., Bellazzini, M., & Correnti, M. 2013, ApJ, 765, LL15

Kinman, T. D., Suntzeff, N. B., & Kraft, R. P. 1994, AJ, 108, 1722

Law, D. R., Johnston, K. V., & Majewski, S. R. 2005, ApJ, 619, 807

Law, D. R., Majewski, S. R., & Johnston, K. V. 2009, ApJ, 703, L67

Law, D. R., & Majewski, S. R. 2010, ApJ, 714, 229

Machado, R. E. G., & Athanassoula, E. 2010, MNRAS, 406, 2386

Monari, G., Antoja, T., & Helmi, A. 2012, European Physical Journal Web of Conferences, 19, 07007

Morrison, H. L., Helmi, A., Sun, J., et al. 2009, ApJ, 694, 130

Navarro, J. F., Frenk, C. S., & White, S. D. M. 1997, ApJ, 490, 493

Perryman, M. A. C., de Boer, K. S., Gilmore, G., et al. 2001, A&A, 369, 339

Rojas-Niño, A.,Valenzuela, O., Pichardo, B., & Aguilar, L. A. 2012, ApJ, 757, 2

Sanderson, R. E., Helmi, A., & Hogg, D. W. 2014, IAU Symposium, 298, 207

Springel, V., Wang, J., Vogelsberger, M., et al. 2008, MNRAS, 391, 1685

Vera-Ciro, C. A., Sales, L. V., Helmi, A., et al. 2011, MNRAS, 416, 1377

Vera-Ciro, C., & Helmi, A. 2013, ApJ, 773, LL4

Vogelsberger, M., White, S. D. M., Helmi, A., & Springel, V. 2007, MNRAS, 385, 236-254

Wetzel, A. R. 2011, MNRAS, 412, 49